In-situ transmission electron microscopy study of thermal stability and carbide formation in amorphous Cu-Mn/C films for interconnect applications

K.H. Nagy*, F. Misják

Centre for Energy Research, Hungarian Academy of Sciences, 1525 Budapest, P.O. Box 49, Hungary

ARTICLE INFO

ABSTRACT

In this study, the thermal stability and Mn carbide formation were investigated in amorphous Cu-Mn/C films with potential applications as interconnect layers. Amorphous Cu-Mn films (with 50 and 70 at% Mn content) were deposited by direct current (DC) magnetron sputtering at room temperature. Evaporated carbon foils were used as substrates to model low-κ carbon doped oxides in their reaction with Cu-Mn films. In-situ transmission electron microscopy indicated that the amorphous state was stable below 300 °C, where the films crystallized into Cu(Mn) and α-Mn based solid solutions. The Mn carbide phases appeared at 400 °C where it was accompanied by the disappearance of the α-Mn phase and a decrease in the Mn content of the Cu(Mn) phase. The $Mn_{23}C_6$ and Mn_5C_2 carbide phases were present from 400 °C to 500 °C, and Mn_5C_2 and Mn_7C_3 carbides in the temperature range of 500–600 °C. The Mn_5C_2 carbides exhibited significant grain growth in the temperature range of 400–600 °C. The activation energies for Mn_5C_2 growth were 101 ± 20 and 88 ± 22 kJ/mol in the films containing 50 and 70 at% Mn, respectively, thereby indicating that growth was facilitated by a higher Mn content. In addition to carbide formation, surface oxidation occurred in the system. Thermodynamic considerations indicate that Mn carbide formation can only occur in the Cu-Mn-C-O system when the Mn is not fully oxidized and free metallic Mn atoms remain.

1. Introduction

Due to the continued downscaling of ultra-large scale integrated circuits, the use of conventional barriers in Cu metallization has become challenging, and thus self-forming barriers (SFB) have been proposed as a potential solution. The basic idea of SFBs involves the formation of a barrier from the material undergoing metallization while it interacts with the dielectric. In particular, Cu metallization involves alloying with a strong oxide-forming element, which is selected because it tends to migrate to the alloy/dielectric interface and reacts with the dielectric. The segregation and reaction of the alloying element with the dielectric can be achieved by annealing during technological processes. Among the various alloying candidates, Mn has been investigated widely and it forms a reliable uniform barrier layer on SiO_2 surfaces [1–4].

Barrier formation in low Mn content Cu-Mn films has been studied extensively [2,5,6] but other compositions also merit investigation. In our previous study, the morphology and electrical properties of the Cu-Mn thin film system were mapped as a function of the composition, and an amorphous phase-state was observed in the 40–70 at% Mn interval

[7]. It is considered that an amorphous structure can have several advantages in SFB processes because its structural homogeneity and lack of grain boundaries may help to prevent Cu diffusion. However, amorphous Cu-Mn structures are metastable, so they may crystallize during annealing or due to other thermal effects that occur in technological processes. Therefore, the thermal stability of Cu-Mn amorphous structures should be examined in order to ensure their adaptability for SFB processes.

Another important issue in the development of ultra-large scale integrated circuits is the optimization of low dielectric constant (κ) insulating materials, which have recently been investigated extensively [8–14]. Among the commercially available low-κ dielectrics, carbon doped oxides (CDOs) are considered to be most compatible with modern device fabrication. CDOs are SiO_2-based materials, which are formed by replacing some of the Si-O bonds with less polar Si-CH_x bonds. However, Si-CH_x bonds are considerably weaker than Si-O bonds and a wide range of device fabrication steps, including barrier formation, can deplete carbon from CDOs and increase the κ value. The released carbon can interfere with the uniform formation of a barrier at the interconnect/CDO interface by forming carbide phases that are

incorporated into the barrier. Some studies of Cu(Mn)-based barrier formation on CDO substrates also investigated how to prevent carbide formation [10,12–14]. These studies modeled barrier formation by depositing a ~1 nm thick Mn layer on CDO substrates with different experimental parameters.

Many studies have investigated the effects of Mn oxidation on Mn carbide formation (e.g., the Mn layer was deposited in an O_2 atmosphere) [10,12,13]. Limited carbide formation was found when the Mn was partially oxidized [12,13], whereas carbide formation was suppressed at full oxidation, even after annealing [10]. However, fully oxidizing the Mn is undesirable because the presence of metallic Mn is important for controlling the thickness of the barrier layer [3]. Other studies aimed to modify the surface of the CDO substrate before Mn deposition. If carbon is removed from the CDO surface by atomic oxygen treatment, a SiO_2-like surface sublayer forms [14]. This sublayer effectively prevents the formation of Mn-C bonds on a non-porous substrate, even after annealing, but it is ineffective on a porous substrate. Furthermore, atomic oxygen treatment may negatively impact the formation of a discrete barrier with porous substrates [14]. Thus, these previous studies indicate that processes for preventing carbide formation may be detrimental for the dielectric constant (e.g., low carbon content and porosity of CDOs) and/or the SFB process (e.g., fully oxidizing the Mn).

In this study, to facilitate the design of SFBs, we studied the reaction between a promising SFB material and carbon. In particular, we investigated the thermal stability of amorphous Cu-Mn films and Mn carbide formation during annealing using in-situ transmission electron microscopy (TEM) analysis. Evaporated carbon foils were used as substrates to model the CDO surfaces in their reaction with Cu-Mn films. Improving our fundamental understanding of Mn carbide formation may assist its prevention, so we characterized the formation of the carbide phases and their grain growth.

2. Experimental

Amorphous Cu-Mn alloy thin films were co-deposited in a high-vacuum direct current (DC) magnetron sputtering system. Films with a thickness of 50 nm were grown at room temperature on evaporated carbon foils. The carbon foils were prepared by thermal sublimation of a graphite rod on collodion film substrates supported by Ni grids at a pressure of Pa. The collodion films were then removed by annealing the grids at 400 °C for 90 min. The resulting carbon foils had an amorphous structure and a thickness of 10–20 nm. The Cu and Mn targets (99.99% and 99.95% purity, respectively) were mounted 25° toward the vertical and the rotating substrate holder was positioned 12 cm away from them. Before deposition, the sputtering chamber was evacuated to a base pressure of 5×10^{-6} Pa and the substrates were annealed at 150 °C for 60 min to remove any mobile hydrocarbons. Ar (99.999% purity) was then introduced at a pressure of 2×10^{-1} Pa. The targets were presputtered before deposition with the shutters closed for 5–10 min. The desired compositions (50 and 70 at% Mn) were obtained by adjusting the magnetrons' power [7]. The deposition rate of the layers was 0.4 nm/s.

The films were annealed in-situ and examined with a Philips CM-20 transmission electron microscope, which operated at 200 keV. The temperature range for in-situ annealing was 20–600 °C and the heat treatment program is shown in Fig. 1. Energy dispersive X-ray spectroscopy (EDS) analysis was performed to verify the compositions of the samples using a Ge detector (NORAN EDS system) attached to the CM-20 microscope.

The phase compositions of the films were evaluated based on the selected area electron diffraction (SAED) patterns using the Process Diffraction program [15]. The size of the area that contributed to the SAED patterns measured 5 µm in diameter. During the evaluation of each SAED pattern, the camera constant was specified by calibrating based on MnO markers. For each temperature step, the MnO lattice
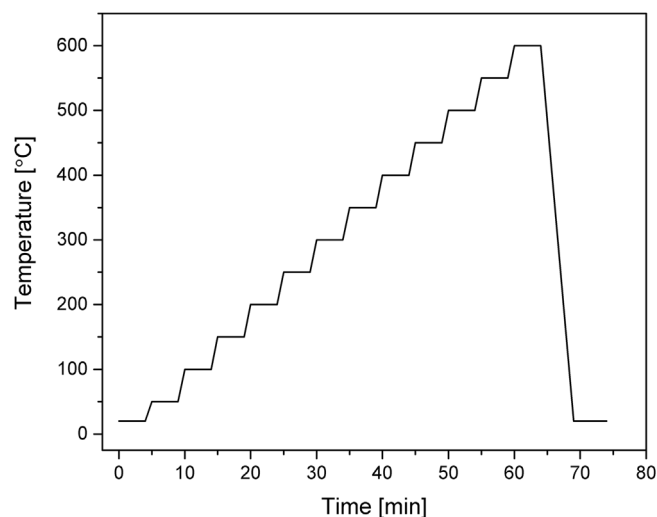

Fig. 1. Annealing cycle used in the in-situ experiments. The vacuum conditions during annealing were 6×10^{-5} Pa at 20 °C, which increased to 1×10^{-3} Pa at 600 °C.

parameter was calculated using Eq. (1):

$$a_T = a_{T=20°C}(1 + \alpha \Delta T),\tag{1}$$

where a_T is the lattice parameter at a given temperature, $\alpha(T)$ is the thermal expansion coefficient, and T is the temperature. The thermal expansion coefficient for MnO was taken from a previous study [16].

3. Results

Figs. 2 and 3 show the changes in the microstructure during annealing based on bright field images and the electron diffraction intensity distributions. The as-deposited films subjected to in-situ heat treatment were amorphous with both compositions [7]. Mn oxidizes readily, even in ultra-high vacuum environments [13], so the presence of MnO nanoparticles caused a slight diffraction contrast (Fig. 2a and e). During annealing, the films with Mn contents of 50 and 70 at% exhibited similar behavior, and only slight differences were observed. As the temperature increased, both films remained amorphous below 300 °C. At 300 °C, both films crystallized into Cu-based and α-Mn-based solid solutions. The typical electron diffraction patterns for these phases are shown in Fig. 4. The grain size in the solid solutions was around 10–40 nm (Fig. 2b and f). The Cu-based solid solution remained stable until the end of annealing, but the Mn-based phases underwent changes. The α-Mn-based solid solution disappeared at 400 °C in the 50 at% Mn film and at 450 °C in the 70 at% Mn content film. New phases appeared at 400 °C (marked by arrows in Fig. 3). In addition, strong oxidation occurred above 400 °C and substantial grain growth was also observed (Fig. 2d and h).

The diffraction maxima determined for the Cu-based and α-Mn-based solid solutions exhibited continuous shifts in both films (Fig. 3), thereby indicating changes in the lattice parameters. The lattice parameters measured for both solid solutions at each temperature are listed in Table 1. In general, two mechanisms can contribute to changes in the lattice parameter: thermal expansion and changes in the solute concentration. Thermal expansion can be calculated based on the lattice parameter for pure components at room temperature ($a_{Cu} = 3,6149$Å [17] and $a_{\alpha-Mn} = 8,9125$Å [18]) and their thermal expansion coefficients ($\alpha_{Cu} = 1.65 \times 10^{-5}1/K$ [17] and $\alpha_{Mn} = 2.17 \times 10^{-5}1/K$ [18]) using Eq. (1). The dissolution limits of each component should be considered when determining changes in the solute concentration. α-Mn can dissolve up to ~10 at% Cu under non-equilibrium conditions [7], ~5 at% C in the temperature range of 0–400 °C [19], and a negligible amount of O [20]. Thus, the α-Mn solid solution could comprise several elements:
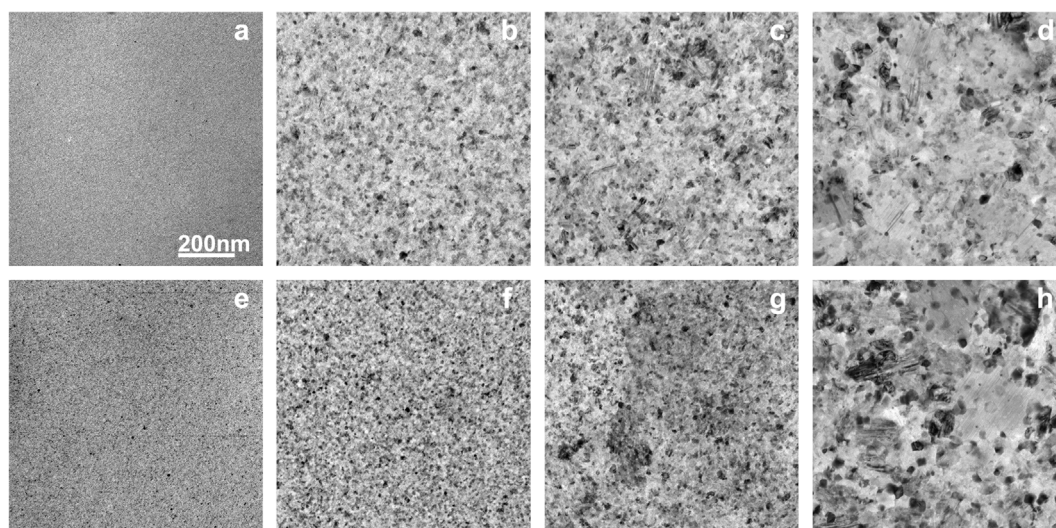
Fig. 2. Changes in the microstructure of the films with Mn contents of 50 at% (a–d) and 70 at% (e–h) during annealing in bright field TEM images (a, e: 20 °C; b, f: 300 °C; c, g: 450 °C; d, h: 600 °C).

Mn, Cu, and C atoms. By contrast, Cu dissolves ~ 20–45 at% Mn in the temperature range of 300–600 °C [21] and negligible amounts of C and O [22,23]. Thus, Cu forms a simple Cu(Mn) solid solution and its composition can be calculated from the lattice parameter. Czigány et al. measured the dependence of the Cu(Mn) lattice parameter based on the composition in sputtered Cu-Mn thin films at room temperature as: $a = a_{Cu} + 0.322c$, where c is the Mn concentration in the Cu(Mn) solid solution in at% [24]. We modified this equation to consider thermal expansion:

$$a_T = a_{Cu_T} + 0.322c,\qquad(2)$$

where a_{Cu_T} is calculated at each temperature using Eq. (1).

Fig. 5 shows the compositions of the Cu(Mn) phase calculated (using Eq. (2)) in the temperature range of 300–600 °C. There were significant declines in the Mn contents in both films. After crystallization, the Cu(Mn) phase dissolved 31 and 23 at% Mn in the films with Mn contents of 50 and 70 at%, respectively, and the Mn content increased slightly in both films as the temperature increased. The Mn content decreased to 18 at% at 400 °C and then decreased further to 6 at% at 450 °C in the film containing 50 at% Mn. In the film containing 70 at% Mn, the Mn content increased at 400 °C but decreased to 9 at% at 450 °C. Above

450 °C, the Mn content varied between 7 and 11 at% in both films.

Fig. 6 shows enlargements of the diffraction intensity distributions for the films with Mn contents of 50 (a) and 70 at% (b) to highlight the formation of the new phases. At 400 °C, two Mn carbide phases could be identified in both films: $Mn_{23}C_6$ and Mn_5C_2. In addition, Mn_5C_2 was present up to 600 °C, but $Mn_{23}C_6$ disappeared at 500 °C and 550 °C in the films with Mn contents of 50 and 70 at%, respectively. At 500 °C, a new carbide, Mn_7C_3, formed in both films and remained stable up to 600 °C. The appearance and disappearance of the crystalline phases are shown in Table 2.

To interpret the carbide formation process, we next provide a comprehensive summary of all the processes that occurred in the multicomponent system. At 400 °C, three processes started simultaneously: the α-Mn phase disappeared (i), the Mn content of the Cu(Mn) phase decreased (ii), and Mn carbides formed (iii). All three processes could be derived from a solid state reaction between the film and the carbon substrate layer. Carbon atoms diffused into the film where they could react with the metallic Mn present in the α-Mn and Cu(Mn) solid solutions to form Mn carbide phases. A slight difference was found between the films containing 50 and 70 at% Mn. In the film containing 70 at% Mn, the α-Mn phase disappeared and the Mn content of the Cu
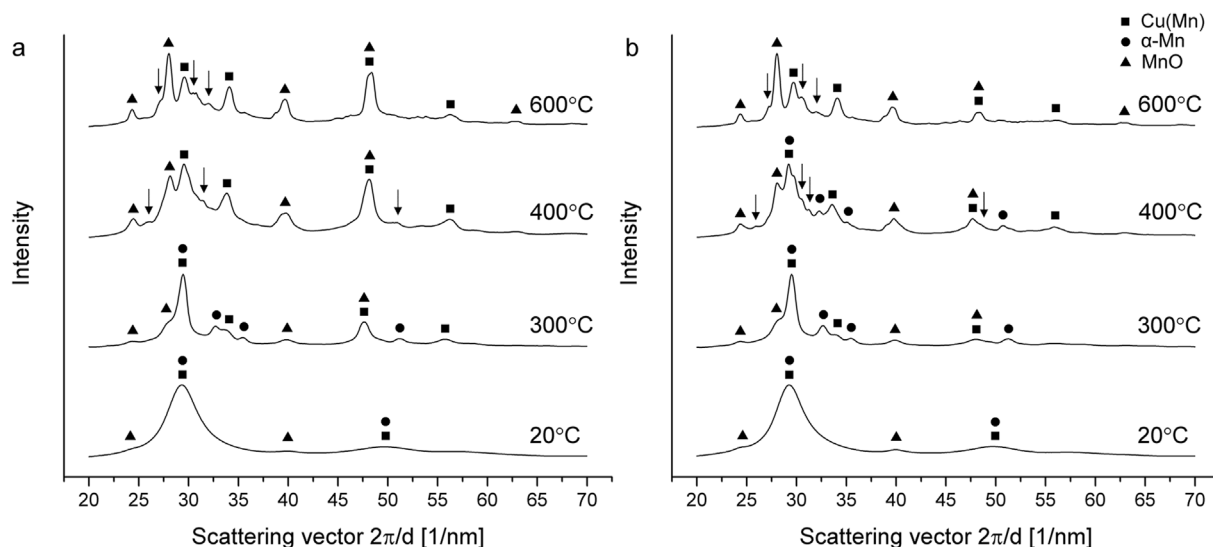

Fig. 3. Electron diffraction intensity distributions for the films with Mn contents of 50 (a) and 70 at% (b) at different temperatures during in-situ heat treatment.
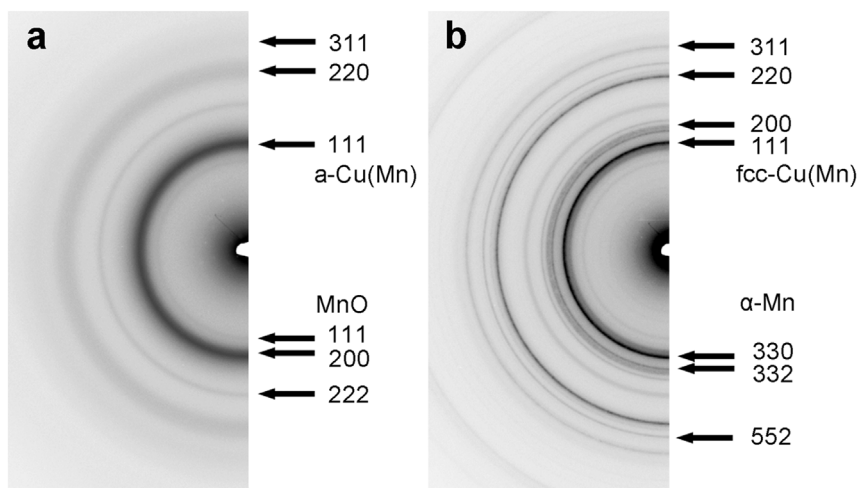
Fig. 4. Selected area electron diffraction patterns obtained for the 50 at% Mn film at 250 °C (a) and 300 °C (b). The structure of the film was amorphous below 300 °C (a). At 300 °C, the film crystallized into Cu-based and α-Mn-based solid solutions (b).

Table 1
Lattice parameters measured for Cu-based and Mn-based solid solutions. The error in the lattice parameter measurements was 0.5%.

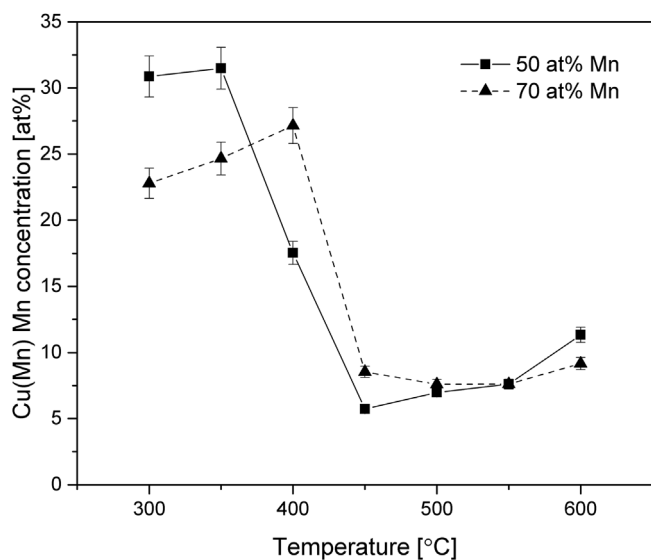| T [°C]	50 at% Mn		70 at% Mn	
	a_{Cu} [Å]	$a_{\alpha-Mn}$ [Å]	a_{Cu} [Å]	$a_{\alpha-Mn}$ [Å]
300	3.731	9.015	3.705	9.015
350	3.736	9.015	3.714	9.015
400	3.694	–	3.725	8.986
450	3.659	–	3.668	–
500	3.666	–	3.668	–
550	3.671	–	3.671	–
600	3.686	–	3.679	–

Fig. 5. Dependence on temperature of the Mn concentration in the Cu(Mn) solid solution for films with Mn contents of 50 and 70 at%.

(Mn) phase decreased at a higher temperature (450 °C), whereas carbides were formed at the same temperature (400 °C) as in the film containing 50 at% Mn. If we assume that carbon diffusion was similar in the two films, the transformation of metallic Mn into carbide must have been prolonged in the film with a Mn content of 70 at% due to its higher Mn content.

Mn can form various carbide phases and three were identified in both films: $Mn_{23}C_6$, Mn_5C_2, and Mn_7C_3. Although we obtained a multicomponent system, the Mn-C phase diagram (shown in Fig. 7) may help to interpret the changes in the carbide phases. In terms of carbides, below 500 °C, the system was in the phase range denoted by I in Fig. 7 where $Mn_{23}C_6$ and Mn_5C_2 carbides were present. As the temperature increased, more carbon diffused into the film and the compound with a lower C:Mn ratio ($Mn_{23}C_6$) disappeared, and a new phase with a higher C:Mn ratio then appeared, i.e., Mn_7C_3. Thus, above 500 °C, the system was in the phase range denoted by II where Mn_5C_2 and Mn_7C_3 carbides were present.

To investigate the microstructure of the carbides, dark field images were recorded using the reflections located between the two dashed lines in Fig. 6. The carbide grains (shown in Fig. 8) had a lamellar structure and they exhibited significant grain growth in the temperature range of 400–600 °C (also shown in Fig. 2c and d, 2g–h). We followed the growth of five carbide grains in dark field images taken at different temperatures within an area of $1.7 \times 1.5 \, \mu m^2$. The grains had a somewhat elongated shape so two perpendicular axes, x and y, were measured on each grain and the grain size d was calculated as: $d = (x + y)/2$. The only carbide phase present throughout the temperature range of 400–600 °C was the Mn_5C_2 phase, so we can conclude that we measured these grains.

Fig. 9a shows the dependence of the grain size measured for the Mn_5C_2 phase as a function of the annealing temperature. The location of the points suggests Arrhenius-type grain growth. The characteristic activation energy for the Arrhenius-type growth process can be estimated according to the following equation [25]:

$$d_g{}^m = d_0{}^m + At^n \exp\left(-\frac{Q_{gg}}{RT}\right), \tag{3}$$

where d_g is the average carbide grain size at a given annealing step (nm), d_0 is the average carbide grain size at the start of each annealing step (nm), t is the time (s), Q_{gg} is the activation energy of carbide grain growth (J/mol), R is the gas constant (J/mol K), T is the absolute temperature (K), and m, A, and n are constants, where $m = 2$ applies when the growth rate is limited by interfacial reactions (ideal grain growth) and $m = 3$ applies for a system limited by the diffusion of atoms in the solid or liquid phases [26]. In our films, carbide growth was presumably limited by the diffusion of Mn and C atoms, so we used $m = 3$. According to the implementation of the experiment, t could be regarded as constant so Eq. (3) can be simplified as follows.

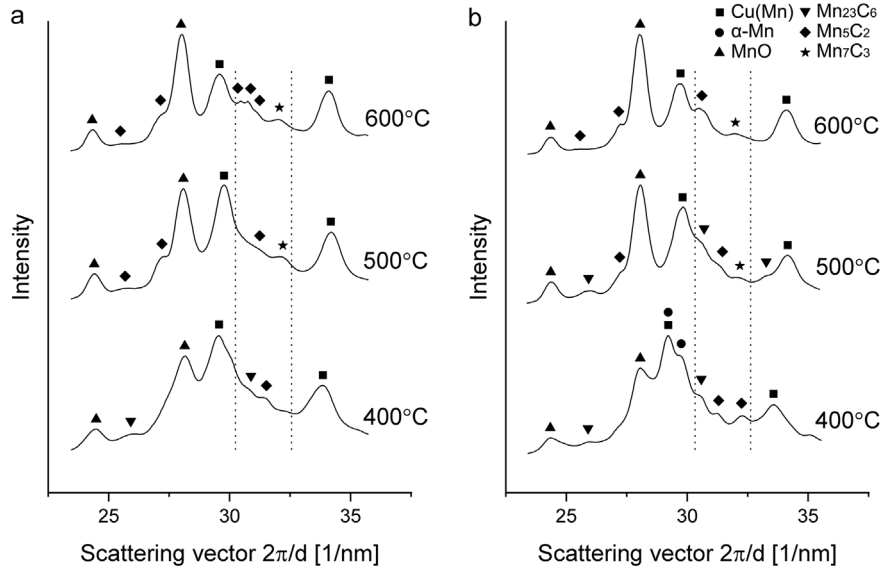$$d_g{}^m = d_0{}^m + A' \exp\left(-\frac{Q_{gg}}{RT}\right) \tag{4}$$

Fig. 6. Electron diffraction intensity distributions determined for the films with Mn contents of 50 at% (a) and 70 at% (b), highlighting carbide formation. The dashed lines denote the angular intervals of the reflections used for dark field TEM images (an example is shown in Fig. 8b).

By calculating the logarithm of Eq. (4), we obtain:

$$\ln(d_g{}^m - d_0{}^m) = lnA' + \left(-\frac{Q_{gg}}{RT}\right). \tag{5}$$

By taking the partial derivative of Eq. (5) with respect to $1/T$, the activation energy can be calculated as follows.

$$\frac{\partial(\ln(d_g{}^m - d_0{}^m))}{\partial(1/T)} = -\frac{Q_{gg}}{R} \tag{6}$$

By plotting Eq. (5) (see Fig. 9b), the relationship between $\ln(d_g{}^m - d_0{}^m)$ and $1/T$ is linear when $m = 3$. Thus, in agreement with our assumption, the grain growth was an Arrhenius-type process, and it was limited by diffusion and the slopes of the linear fits were equal to Q_{gg}/R (Eq. (6)). Thus, the activation energies for Mn_5C_2 grain growth were 101 ± 20 and 88 ± 22 kJ/mol in the films containing 50 and 70 at% Mn, respectively. Therefore, carbide growth was facilitated by higher Mn contents.

In addition to carbide formation, surface oxidation occurred in the system. MnO was present at the top of the as-deposited films but the intensity of the MnO diffraction peaks (Fig. 2) increased significantly during annealing above 300 ˚C. To compare the probability of oxide and carbide formation, the standard free energy (ΔG^0) was determined for each of the two processes in the annealing temperature range. The carbon line [27] divides all oxides into two classes. The oxides with more negative standard free energy than the carbon line cannot be reduced by carbon. The carbon line was at a constant value of -395 kJ/mol in the temperature range of 20–600 ˚C [27], and the MnO curve varied in a linear manner from -729 kJ/mol to -640 kJ/mol

[28]. The standard free energy curve for MnO was below the carbon line, so the carbon could not reduce MnO. Therefore, Mn carbide formation could only occur in this multicomponent system when free metallic Mn atoms were present.

This thermodynamic restriction explains the results of previous studies that investigated the effects of Mn oxidation on Mn carbide formation [10,12,13]. Bogan et al. and McCoy et al. [12,13] found that the partial oxidation of Mn resulted in limited Mn carbide formation. In addition, Casey et al. [10] showed that the full oxidation of Mn effectively inhibited Mn carbide formation, although it increased the thickness of the barrier layer. In a later study, Bogan et al. [14] investigated another method for preventing Mn carbide formation, where they modified the surface of the CDO substrate and created an SiO_2-like surface sublayer, which avoided Mn carbide formation on a non-porous CDO. However, limited carbide formation was found on a porous substrate and the surface treatment had detrimental effects on the formation of a discrete barrier layer.

Based on the experimental results and thermodynamic arguments, we provide suggestions regarding the requirements in terms of the optimal method for inhibiting carbide formation. First, in the environment of the Cu(Mn)/CDO interface, there must be sufficient oxygen for the full oxidation of Mn. Second, the diffusion of Mn into the CDO must be prevented.

4. Summary

Amorphous Cu-Mn thin films (with Mn contents of 50 and 70 at%) were deposited by DC magnetron sputtering on evaporated carbon

Table 2
Phases of the films with Mn contents of 50 and 70 at% in the temperature range of 300–600 ˚C (plus signs indicate that a given phase exists at a given temperature).

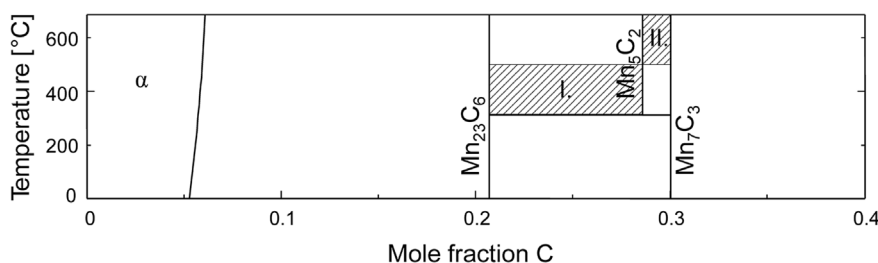| T [˚C]	Cu		α-Mn		$Mn_{23}C_6$		Mn_5C_2		Mn_7C_3		MnO	
	50%	70%	50%	70%	50%	70%	50%	70%	50%	70%	50%	70%
300	+	+	+	+							+	+
350	+	+	+	+							+	+
400	+	+		+	+	+	+	+			+	+
450	+	+			+	+	+	+			+	+
500	+	+				+	+	+	+	+	+	+
550	+	+					+	+	+	+	+	+
600	+	+					+	+	+	+	+	+

Fig. 7. Mn-C equilibrium phase diagram in the temperature range of 0–650 °C based on Ref. [19].
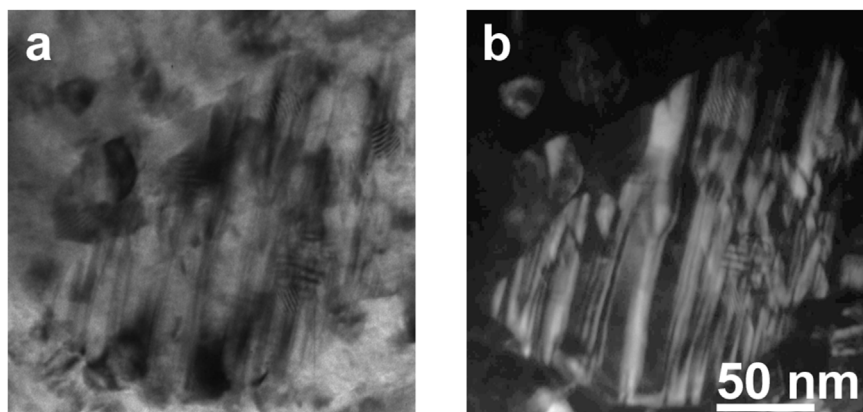

Fig. 8. Bright field (a) and dark field (b) image of a Mn_5C_2 carbide grain in the 50 at% Mn sample annealed at 600 °C.

substrates at room temperature. The films were annealed in-situ in the TEM to investigate the thermal stability of the amorphous Cu-Mn films and Mn carbide formation. Both compositions exhibited similar behavior during annealing. The amorphous state was stable below 300 °C, where the films crystallized into Cu(Mn) and α-Mn-based solid solutions. The Cu-based solid solution remained stable up to 600 °C but the Mn-based phases underwent changes. The Mn carbide phases appeared at 400 °C, which were accompanied by the disappearance of the α-Mn phase and a decrease in the Mn content of the Cu(Mn) phase. In the temperature range of 400–500 °C, the $Mn_{23}C_6$ and Mn_5C_2 carbide phases were present. As the temperature increased, more carbon diffused into the film. Hence, the compound with a lower C:Mn ratio ($Mn_{23}C_6$) disappeared and a new phase with a higher C:Mn ratio appeared, i.e., Mn_7C_3. The Mn_5C_2 carbides had a lamellar structure and they exhibited Arrhenius-type grain growth in the temperature range of

400–600 °C. The activation energies for Mn_5C_2 growth were 101 ± 20 and 88 ± 22 kJ/mol in the films containing 50 and 70 at% Mn, respectively, thereby indicating that carbide growth was facilitated by higher Mn contents. In addition to carbide formation, surface oxidation also occurred in the system. Our results suggest that a thin, uniform barrier layer without carbide formation can be formed on the surfaces of CDOs when sufficient oxygen is available for the full oxidation of Mn within the diffusion distance of the Cu(Mn)/CDO interface and when the diffusion of Mn into the CDO is prevented.

Prime novelty statement

In the submitted manuscript, we report in-situ TEM results obtained on thermal stability and solid phase reaction between amorphous Cu-Mn films and carbon substrates. Carbon substrates are used to model
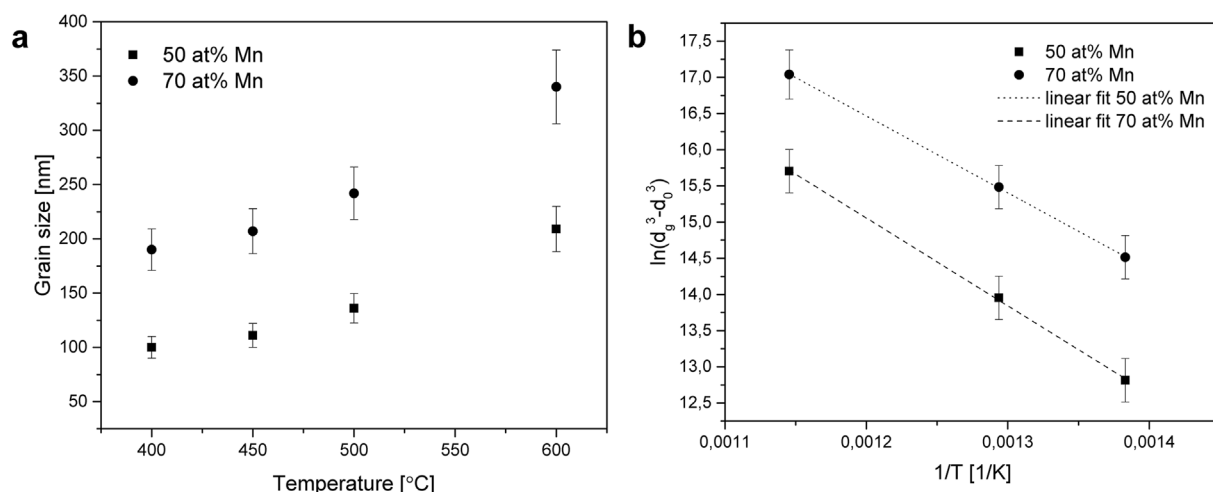

Fig. 9. Mn_5C_2 grain growth during annealing. Dependence of the grain size as the function of the annealing temperature (a). Dependence of the logarithm of grain growth ($d_g{}^m - d_0{}^m$) as a function of $1/T$ when $m = 3$ (Eq. (6)) (b).

low-κ carbon doped dielectric surfaces in their reaction with Cu-Mn films. The goal is to describe the mechanism of Mn carbide formation and the forming carbide phases. The possibility of suppressing carbide formation is discussed.

Acknowledgments

References

[1] J. Koike, M. Wada, Self-forming diffusion barrier layer in Cu–Mn alloy metallization, Appl. Phys. Lett. 87 (2005) 41911 https://dx.doi.org/10.1063/1.1993759.

[2] M. Haneda, J. Iijima, J. Koike, Growth behavior of self-formed barrier at Cu–Mn/SiO2 interface at 250–450°C, Appl. Phys. Lett. 90 (2007) 252107 https://dx.doi.org/10.1063/1.2750402.

[3] P. Casey, J. Bogan, J.G. Lozano, P.D. Nellist, G. Hughes, Chemical and structural investigation of the role of both Mn and Mn oxide in the formation of manganese silicate barrier layers on SiO2, J. Appl. Phys. 110 (2011) 54507 https://doi.org/10.1063/1.3630123.

[4] C. Byrne, B. Brennan, A.P. McCoy, J. Bogan, A. Brady, G. Hughes, In situ XPS chemical analysis of MnSiO₃ copper diffusion barrier layer formation and simultaneous fabrication of metal oxide semiconductor electrical test MOS structures, ACS Appl. Mater. Interfaces 8 (2016) 2470–2477, http://dx.doi.org/10.1021/acsami.5b08044.

[5] J.G. Lozano, J. Bogan, P. Casey, A.P. McCoy, G. Hughes, P.D. Nellist, Scanning transmission electron microscopy investigations of self-forming diffusion barrier formation in Cu(Mn) alloys on SiO2, Apl. Mater. 1 (2013) 42105 https://dx.doi.org/10.1063/1.4822441.

[6] M.P. Nguyen, Y. Sutou, J. Koike, Diffusion barrier property of MnSixOy layer formed by chemical vapor deposition for Cu advanced interconnect application, Thin Solid Films 580 (2015) 56–60 https://doi.org/10.1016/j.tsf.2015.03.007.

[7] F. Misják, K.H. Nagy, P. Lobotka, G. Radnóczi, Electron scattering mechanisms in Cu-Mn films for interconnect applications, J. Appl. Phys. 116 (2014) 83507 https://dx.doi.org/10.1063/1.4893718.

[8] J.M. Ablett, J.C. Woicik, Z. Tőkei, S. List, E. Dimasi, Phase identification of self-forming Cu–Mn based diffusion barriers on p-SiOC: H and SiO2 dielectrics using x-ray absorption fine structure, Appl. Phys. Lett. 94 (2009) 42112 https://dx.doi.org/10.1063/1.3068500.

[9] C.J. Wilson, H. Volders, K. Croes, M. Pantouvaki, G.P. Beyer, A.B. Horsfall, A.G. O'Neill, Z. Tőkei, In situ X-ray diffraction study of self-forming barriers from a Cu–Mn alloy in 100 nm Cu/low-k damascene interconnects using synchrotron radiation, Microelectron. Eng. 87 (2010) 398–401 https://dx.doi.org/10.1016/j.mee.2009.06.023.

[10] P. Casey, J. Bogan, G. Hughes, Photoemission study of carbon depletion from ultralow-κ carbon doped oxide surfaces during the growth of Mn silicate barrier layers, J. Appl. Phys. 110 (2011) 124512 https://dx.doi.org/10.1063/1.3669998.

[11] T.K. Indukuri, R.N. Akolkar, J.S. Clarke, A. Genc, F. Gstrein, M.C. Harmes, B. Miner, F. Xia, D.J. Zierath, S. Balakrishnan, Electrical and reliability characterization of CuMn self forming barrier interconnects on low-k CDO dielectrics, Microelectron. Eng. 92 (2012) 49–52 https://dx.doi.org/10.1016/j.mee.2011.04.043.

[12] J. Bogan, A.P. McCoy, R. O'Connor, P. Casey, C. Byrne, G. Hughes, Photoemission study of the identification of Mn silicate barrier formation on carbon containing low-κ dielectrics, Microelectron. Eng. 130 (2014) 46–51 https://doi.org/10.1016/j.mee.2014.09.012.

[13] A.P. McCoy, J. Bogan, L. Walsh, C. Byrne, R. O'Connor, J.C. Woicik, G. Hughes, The impact of porosity on the formation of manganese based copper diffusion barrier layers on low- κ dielectric materials, J. Phys. D Appl. Phys. 48 (2015) 325102 https://doi.org/10.1088/0022-3727/48/32/325102.

[14] J. Bogan, R. Lundy, A.P. McCoy, R. O'Connor, C. Byrne, L. Walsh, P. Casey, G. Hughes, In-situ surface and interface study of atomic oxygen modified carbon containing porous low-κ dielectric films for barrier layer applications, J. Appl. Phys. 120 (2016) 105305 https://doi.org/10.1063/1.4962371.

[15] J.L. Lábár, Consistent indexing of a (set of) single crystal SAED pattern(s) with the Process Diffraction program, Ultramicroscopy 103 (2005) 237–249 https://dx.doi.org/10.1016/j.ultramic.2004.12.004.

[16] I. Suzuki, S. Okajima, K. Seya, Thermal expansion of single-crystal manganosite, J. Phys. Earth 27 (1979) 63–69 https://doi.org/10.4294/jpe1952.27.63.

[17] Technical data for Cu, (2017). http://periodictable.com/Elements/029/data.html (accessed September 20, 2017).

[18] Technical data for Mn, (2017). http://periodictable.com/Elements/025/data.html (accessed September 20, 2017).

[19] M.-K. Paek, J.-J. Pak, Y.-B. Kang, Phase equilibria and thermodynamics of Mn–C, Mn–Si, Si–C binary systems and Mn–Si–C ternary system by critical evaluation, combined with experiment and thermodynamic modeling, Calphad 46 (2014) 92–102 https://doi.org/10.1016/j.calphad.2014.02.007.

[20] A.N. Grundy, B. Hallstedt, L.J. Gauckler, Assessment of the Mn-O system, J. Phase Equil. 24 (2003) 21–39 https://doi.org/10.1007/s11669-003-0004-6.

[21] C.P. Wang, X.J. Liu, I. Ohnuma, R. Kainuma, K. Ishida, Thermodynamic assessments of the Cu–Mn–X (X: Fe, Co) systems, J. Alloy. Comp. 438 (2007) 129–141 https://dx.doi.org/10.1016/j.jallcom.2006.08.018.

[22] C-Cu phase diagram, (2017). http://www.crct.polymtl.ca/fact/phase_diagram.php?file=C-Cu.jpg&dir=SGTE2014 (accessed September 20, 2017).

[23] L. Schramm, G. Behr, W. Löser, K. Wetzig, Thermodynamic reassessment of the Cu-O phase diagram, J. Phase Equilibria Diffusion 26 (2005) 605–612 https://doi.org/10.1007/s11669-005-0005-8.

[24] Z. Czigány, F. Misják, O. Geszti, G. Radnóczi, Structure and phase formation in Cu–Mn alloy thin films deposited at room temperature, Acta Mater. 60 (2012) 7226–7231 https://doi.org/10.1016/j.actamat.2012.09.034.

[25] L. Wang, D. Qian, J. Guo, Y. Pan, Austenite grain growth behavior of AISI 4140 alloy steel, Adv. Mech. Eng. 5 (2013), https://doi.org/10.1155/2013/762890.

[26] C. Wagner, Theorie der Alterung von Niederschlägen durch Umlösen, Electrochemistry 65 (1961) 581–591, http://dx.doi.org/10.1002/bbpc.19610650704.

[27] G.R. Gaskell, Metallurgical thermodynamics, in: R.W. Cahn, P. Haasen (Eds.), Phys. Metall. North-Holland, 1996, pp. 432–433.

[28] K.T. Jacob, A. Kumar, Y. Waseda, Gibbs Energy of formation of MnO: measurement and assessment, J. Phase Equilibria Diffusion 29 (2008) 222–230 https://doi.org/10.1007/s11669-008-9280-5.